(2)

1. Agency Use	3. Report Type and Dates Covered. Final - Journal Article

4. Title and Subtitle.
Hindcasting of Wind-Driven Anomalies Using a Reduced-Gravity Global Ocean Model

5. Funding Numbers.

Contract	
Program Element No.	0602435N
Project No.	3584
Task No.	MOG
Accession No.	DN650751
Work Unit No.	93232C

6. Author(s).
E. Joseph Metzger, Harley E. Hurlburt, John C. Kindle, Ziv Sirkes*, and James M. Pringle**

7. Performing Organization Name(s) and Address(es).
Naval Oceanographic and Atmospheric Research Laboratory
Ocean Science Directorate
Stennis Space Center, MS 39529-5004

8. Performing Organization Report Number.
JA 323:049:92

9. Sponsoring/Monitoring Agency Name(s) and Address(es).
Naval Oceanographic and Atmospheric Research Laboratory
Exploratory Development Program Group
Stennis Space Center, MS 39529-5004

10. Sponsoring/Monitoring Agency Report Number.
JA 323:049:92

11. Supplementary Notes.
Published in Marine Technology Society Journal
*Institute for Naval Oceanography, Stennis Space Center, MS
**Planning Systems Inc., Slidell LA

12a. Distribution/Availability Statement.
Approved for public release; distribution is unlimited.

12b. Distribution Code.

13. Abstract *(Maximum 200 words).*

Global versions of the Navy Layered Ocean Model are used to hindcast wind-driven oceanic anomalies. These versions are reduced-gravity with with lowest layer infinitely deep and and at rest, and grid resolutions of 1/2° and 1/4° are used. Winds at the 1000 millibar level from the European Centre for Medium-Range Weather Forecasts (ECMWF) are used as forcing functions for the models over the 1981 to 1989 time frame. The ability of the models to reproduce wind-forced anomalies on intraseasonal to interannual time scales is studied by comparing the model solutions with various observational data sets. These include satellite altimetry data, drifting buoy data, and island and coastal sea level data. The effects of varying horizontal and vertical resolution are also detailed. The models are able to hindcast many of the wind-driven anomalies; the best correlations is found in the tropical regions where the oceanic anomalies. However, the resolution of the global models used here is not adequate for these. In addition the reduced-gravity models lack the barotropic mode and realistic bottom topography, which can play an important role in the flow instabilities.

14. Subject Terms.	15. Number of Pages.
Ocean models, ocean forecasting, fronts, air-sea interaction	10
	16. Price Code.

17. Security Classification of Report.	18. Security Classification of This Page.	19. Security Classification of Abstract.	20. Limitation of Abstract.
Unclassified	Unclassified	Unclassified	SAR

Marine Technology Society

JOURNAL

VOLUME 26
NUMBER 2
SUMMER 1992

THE INTERNATIONAL, INTERDISCIPLINARY SOCIETY DEVOTED TO OCEAN AND MARINE ENGINEERING, SCIENCE, AND POLICY

Oceanic and Atmospheric Nowcasting and Forecasting

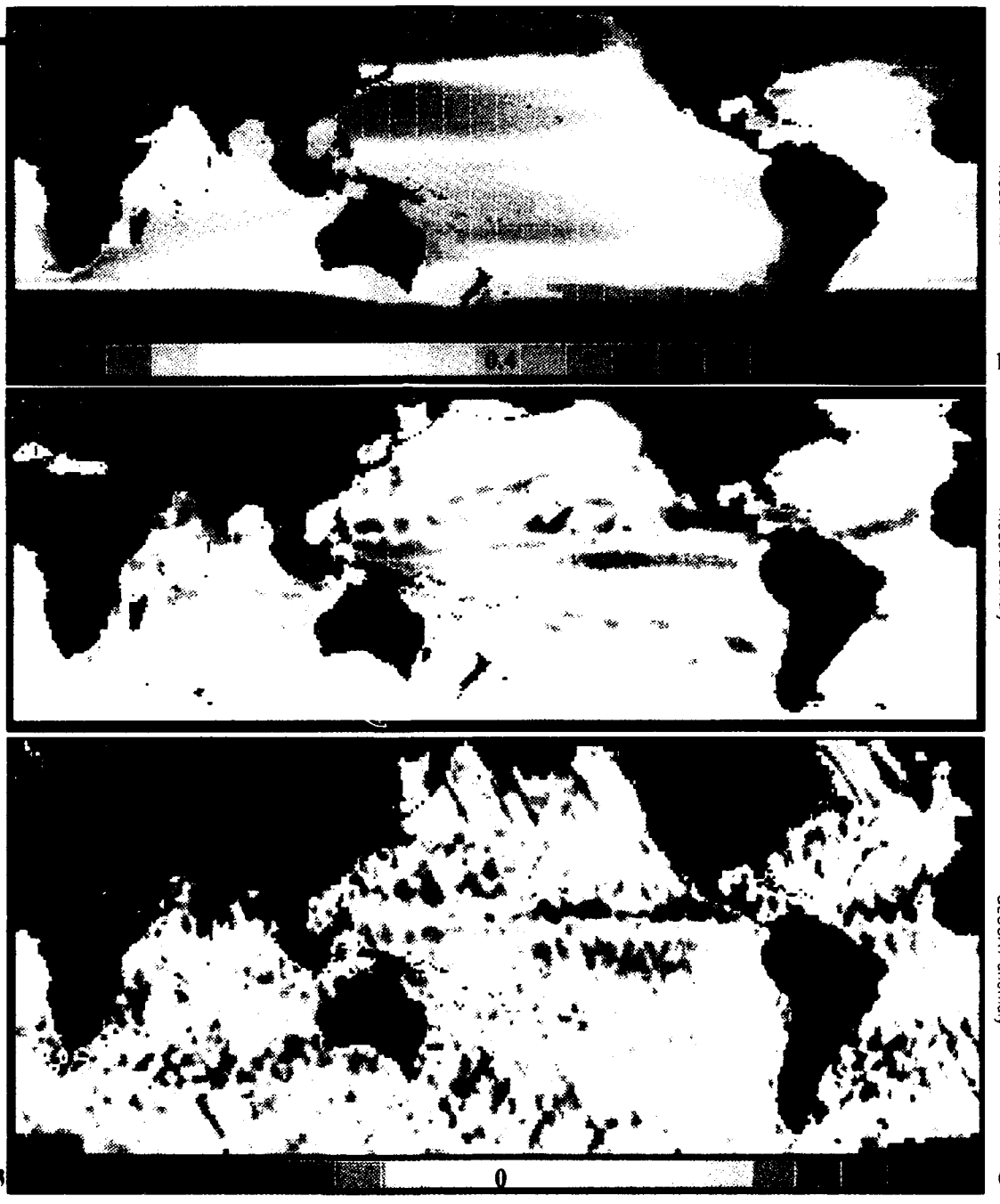

Hindcasting of Wind-Driven Anomalies Using a Reduced-Gravity Global Ocean Model

PAPER

E. Joseph Metzger
Naval Research Laboratory
Stennis Space Center,
Mississippi

Harley E. Hurlburt
Naval Research Laboratory
Stennis Space Center,
Mississippi

John C. Kindle
Naval Research Laboratory
Stennis Space Center,
Mississippi

Ziv Sirkes
Institute for Naval
Oceanography
Stennis Space Center,
Mississippi

James M. Pringle
Planning Systems, Inc.
Slidell, Louisiana

ABSTRACT

Global versions of the Navy Layered Ocean Model are used to hindcast wind-driven oceanic anomalies. These versions are reduced-gravity with the lowest layer infinitely deep and at rest, and grid resolutions of ½° and ¼° are used. Winds at the 1000 millibar level from the European Centre for Medium-Range Weather Forecasts (ECMWF) are used as forcing functions for the models over the 1981 to 1989 time frame. The ability of the models to reproduce wind-forced anomalies on intraseasonal to interannual time scales is studied by comparing the model solutions with various observational data sets. These include satellite altimetry data, drifting buoy data, and island and coastal sea level data. The effects of varying horizontal and vertical resolution are also detailed. The models are able to hindcast many of the wind-driven anomalies; the best correlation is found in the tropical regions where the oceanic response to atmospheric forcing is the most rapid. At mid-latitudes, mesoscale flow instabilities are a major source of oceanic anomalies. However, the resolution of the global models used here is not adequate for these. In addition, the reduced-gravity models lack the barotropic mode and realistic bottom topography, which can play an important role in the flow instabilities.

INTRODUCTION

Three versions of a global ocean model are used to investigate the ability of wind-driven ocean models to hindcast and to help identify a particular class of wind-forced oceanic anomalies. This is done by forcing the ocean models using an operational atmospheric wind product and then comparing the model response to suitable oceanic observations that are contemporaneous with the atmospheric forcing. No assimilation of *time-dependent* oceanic data is used in the model. As discussed by Hurlburt (1984; 1987), the oceanic anomalies of interest here are a direct integrated response to atmospheric forcing on time scales much longer than the one-week time scale of atmospheric predictability. Therefore, they are insensitive to errors in depicting the daily fluctuations in the weather but are sensitive to errors on monthly and interannual time scales. Other studies of this class of anomalies include Haney (1980) for the mid-latitude North Pacific, Busalacchi et al. (1983) and Cane et al. (1986) for El Niño and the equatorial Pacific, and Pares-Sierra and O'Brien (1989) for sea level along the west coast of North America.

The global ocean models used here are reduced-gravity versions of the Navy Layered Ocean Model, which is a descendant of the primitive equation model by Hurlburt and Thompson (1980) and which has been significantly enhanced by Wallcraft (1991). The model grid covers the globe from 72°S to 71°N. Results from model simulations using two different horizontal resolutions are discussed; they are the ½° model (0.5° lat. by 0.7° long.) and the ¼° model (0.25° lat. by 0.35° long.). This is the resolution for each model variable. Sensitivities to vertical resolution are also presented. The models have either one or three active upper layers while the lowest layer is infinitely deep and at rest. These are commonly referred to as 1.5- and 3.5-layer models because they contain two and four layers respectively but represent only one and three internal vertical modes for the ocean. The mean layer depth is at 250 m for the 1.5-layer model and 135 m, 335 m, and 550 m for the 3.5-layer models. Large deviations from these mean interface depths occur. The models contain realistic coastline geometry and include the deep marginal seas, such as the Bering Sea, the Sea of Okhotsk, the Sea of Japan, the South China Sea, the Sulu Sea, and the Indonesian archipelago. They have horizontal mixing in the form of Laplacian friction and vertical exchange of momentum, mass, and heat. The models are thermodynamic and horizontal density gradients within each layer can be modified by advection, diffusion, entrainment, and relaxation to an annual mean density climatology based on Levitus (1982).

Winds are the only time-dependent forcing for the models and no synoptic ocean data are assimilated. They were spun up from rest to statistical equilibrium using the Hellerman and Rosenstein (1983) (HR) monthly mean wind stress climatology. To drive the model on interannual time scales, 1000 millibar (mb) winds from the European Centre for Medium-Range Weather Forecasts (ECMWF) were used. The combination of global coverage and a relatively consistent long time series led us to choosing the ECMWF winds over those from other operational atmospheric centers. The velocity components at twelve-hour intervals were converted to wind stress using a constant drag coefficient of 1.5×10^{-3} and monthly averages were formed. In forming the surface stresses

Cover Caption
A comparison of sea surface height (SSH) anomalies in the wind-forced ½° 3.5-layer Navy Layered Ocean Model and the U.S. Navy's GEOSAT-ERM. The upper panel is the two-year model mean SSH sampled along GEOSAT-ERM tracks. The middle panel is the model SSH anomaly from the above mean while the lower panel is the GEOSAT-ERM SSH anomaly from its mean over the same period. Both anomalies are from repeat cycle 41 (September 20–October 7, 1988). The color bars are in meters. (See paper by Metzger et al. for discussion.)

from the 1000 mb winds, no directional changes were made. However, global simulations forced by the ECMWF winds yield a southern branch of the South Equatorial Current (SEC) and a South Equatorial Countercurrent (SECC) that are too strong in comparison with observations and a North Equatorial Countercurrent (NECC) that is 1° to 2° north of its observed position. It was determined that a more realistic mean state could be obtained in the ocean model by using a hybrid wind set. The ECMWF mean over the 1981 to 1989 time frame was subtracted from the monthly means and replaced by the HR annual mean. This hybrid wind set (E/H) was used to extend the integration already spun up to statistical equilibrium using the HR monthly winds. Thus, the annual mean solution would still be driven primarily by HR while seasonal and interannual forcing would come from ECMWF. All model results discussed use the E/H wind forcing.

Because the ½° model is basically non-eddy resolving and the ¼° model is only marginally eddy resolving, they do not reproduce realistic mesoscale variability observed in major current systems, such as the Kuroshio Extension or the Gulf Stream. In addition, the reduced-gravity models lack the barotropic mode and realistic bottom topography, which can play an important role in the flow instabilities. These instabilities are the primary cause of the observed mesoscale (~50 to 500 km) variability. However, the model is able to reproduce directly wind-forced anomalies on intraseasonal to interannual time scales. The primary objective of this report is to examine this capability. These wind-forced anomalies include El Niño-Southern Oscillation events, sea level variability, the position of fronts and currents, and current transport variability. The oceanic response to atmospheric forcing is most rapid in the tropics, which is where these wind-forced anomalies are predominantly found.

The model's ability to respond to large-scale wind-forced anomalies is illustrated in the figure on the outside front cover of this issue (Cover 1); shown is a global comparison of sea surface height (SSH) anomalies from the ½° 3.5-layer model and data from the U.S. Navy's Geodesy Satellite-Exact Repeat Mission (GEOSAT-ERM). The GEOSAT-ERM data set was obtained from the National Oceanographic Data Center and was corrected for orbit error using the Goddard Earth Model (GEM-T2) gravity model (Haines et al., 1990) and software developed by Koblinsky et al. (1990). The large-scale orbit error was further reduced using a technique outlined by Sirkes and Wunsch (1990). All data for this comparison have been mapped on a 1° by 1° grid using optimum interpolation.

The upper panel on Cover 1 is the mean SSH from the model over the first forty-three repeat cycles (November 8, 1986 to November 10, 1988) of the GEOSAT-ERM. It was obtained by sampling the model along the seventeen-day repeat tracks of the GEOSAT ERM at the same times as the satellite. The large-scale oceanic gyre systems are clearly evident in all basins, but at subpolar latitudes the model produces a relatively flat SSH field within the interior of the subpolar gyres. This is a result of positive wind stress curl, which raises the interfaces between the layers. To prevent the interfaces from surfacing, vertical mixing is used. Most of the wind energy in these regions with flat SSH is lost to the infinitely deep abyssal layer and the active layers are shallow and flat. Thus the model has no significant geostrophically balanced currents or anomalies in the interior of the subpolar gyres.

The middle panel of Cover 1 shows the model SSH deviation from the mean described above for repeat cycle 41 (September 20 to October 7, 1988), while the bottom panel is the SSH deviation from the GEOSAT-ERM for the same repeat cycle. The GEOSAT-ERM mean was calculated over the same time period as the upper panel. Some striking similarities can be seen between the two anomaly fields. These include a distinctive narrow band of positive anomaly across most of the Pacific Ocean between 5° and 10°N. Negative anomalies appear on either side of it in the central and eastern basin. In the GEOSAT-ERM data one might think this band of positive anomaly is the result of water vapor error associated with the intertropical convergence zone, but the anomaly also appears in the model, which is not subject to that type of error. Both also show relatively high sea level in the western equatorial Pacific Ocean and the tilt of the SSH along the equator is similar. Additionally, a positive anomaly in both data sets is seen to extend into the Indian Ocean off the west coast of Australia.

Similarities between the model SSH deviations and those from GEOSAT-ERM can be seen in other regions, but areas of disagreement also exist. The best agreement is at the low latitudes where there is a relatively rapid response to changes in the wind fields. The worst agreement is in the subpolar latitudes due to the interface ventilation discussed earlier. Some agreement can be found at mid-latitudes even though the model lacks mesoscale variability. Note the positive anomalies in the Kuroshio current region south and east of Japan.

A similar comparison can be found in Hurlburt et al. (1992) for the ½° 1.5-layer global model. The results for the 1.5- and the 3.5-layer models are similar, but a significant difference is found in the eastern equatorial Pacific where the negative (blue) SSH anomaly along the equator is strongest further to the west in the 3.5-layer

FIGURE 1. 1981–1989 mean sea surface height (SSH) field overlayed with currents from the ° 3.5-layer global model. Only a subregion is shown, the Pacific Ocean north of 20°S. The contour interval is 5 cm. Shaded areas represent model land and regions shallower than 200 meters (with a few exceptions).

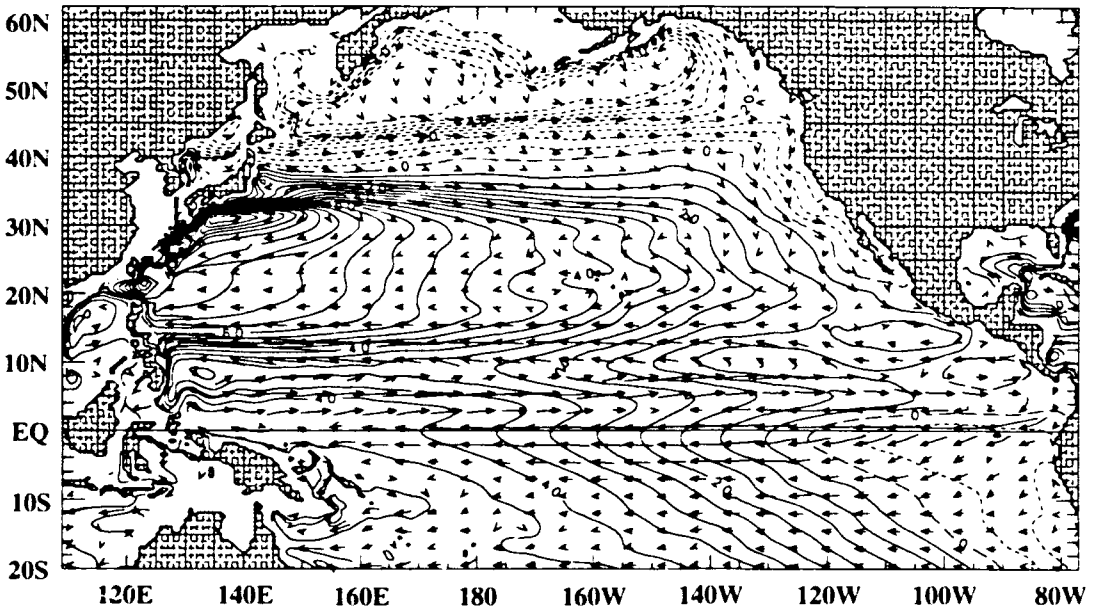

model as observed in the GEOSAT-ERM data. This is due to vertical mixing in the 3.5-layer model associated with the equatorial undercurrent in the eastern Pacific. With only one active layer, the 1.5-layer model cannot have an undercurrent.

These results show the model is able to hindcast observed wind-forced oceanic anomalies, a positive note for the atmospheric forcing from ECMWF as well as the ocean model. Given accurate atmospheric forcing, the model should exhibit intraseasonal to interannual variations similar to those seen in in situ data. After a brief discussion of the model climatology, the remainder of the paper will focus on the tropical latitudes based on the preceding results. Comparisons will be made between the model, drifting buoys, and island and coastal sea level stations.

MODEL CLIMATOLOGY

The discussion of the model climatology will concentrate on the circulation in the Pacific Ocean north of 20°S, since the remaining model-data comparisons are in this basin. Figure 1 shows the 1981 to 1989 mean SSH field overlayed with currents for the ½° 3.5-layer model. With a few exceptions, the mean solution is similar for all the models discussed here.

The large cyclonic subpolar and anticyclonic subtropical gyres are separated by the Subarctic Front at 40° to 45°N. The strongest portion of the subtropical gyre is bounded on the north by the Kuroshio Extension at 32° to 36°N, giving a double frontal structure separating the two gyres. The southern half of the subtropical gyre consists of broad westward return flow, which intensifies to the west and south as the North Equatorial Current (NEC) at 10° to 16°N.

Near the Philippines coast at approximately 14°N, the NEC splits into the northward flowing Kuroshio Current and the southward Mindanao Current (MC). This split point varies by about a degree among the various models, but all are in close agreement with the observed dynamic height from the Navy's Generalized Digital Environmental Model (GDEM) climatology (Teague and Hogan, 1989; Hurlburt et al., 1989); GDEM places the split point near 14.5°N.

In the model the MC flows around the Mindanao Eddy, centered at 5°N, 127°E, and merges with the SEC to form the eastward flowing NECC. The latter is centered near 5°N and extends across the width of the basin. The model shows the SECC at 7° to 10°S, but it is much weaker than the NECC and is confined to west of the dateline. The model also accurately depicts the SSH tilt across the Pacific basin at the equator. Philander (1990) indicates that the observed west to east decrease is approximately 50 cm, the same as the model.

A detailed description of the model climatology in the other ocean basins will not be presented here, but the model is able to represent the basic upper ocean features in these domains. In the Indian Ocean, the reversals of the Arabian Sea and Bay of Bengal current

systems that result from the seasonal monsoonal circulation are depicted; however, the complex eddy structure off the coast of Somalia during the southwest monsoon is not clearly seen in the ½° model. These eddies are better defined in the ¼° model. The large-scale circulation in the Atlantic Ocean is simulated, although the representation of the Gulf Stream is unrealistic. In part, this can be attributed to the lack of the thermohaline circulation and associated deep western boundary currents that play an important role in this basin (Gordon, 1986; Schmitz and Richardson, 1991). In the tropical latitudes, the models depict the retroflection of the Brazil Current near 6° to 8°N.

UPPER OCEAN TRAJECTORY FIELDS

The next model-data comparison focuses on the western equatorial Pacific Ocean where the upper layer current field from the model is compared to that determined from trajectories of drifting buoys drogued at 10 m and acoustic Doppler current profiler (ADCP) data. The observational data were obtained during the Western Equatorial Pacific Ocean Circulation Study III (WEPOCS III) and were analyzed by Lukas et al. (1991); they provide an excellent quasi-synoptic view of the upper ocean. Figure 2a shows the mean July through September 1988 velocity vectors averaged on 1° squares. It includes both drifting buoy and ADCP data and

FIGURE 2. (*a*) Mean July–September 1988 velocity vectors averaged over 1° squares; includes both drifting buoy and ADCP data. (Adapted from Lukas et al., 1991). Upper layer currents averaged over the same time period for (*b*) the ½° 1.5-layer model, (*c*) the ½° 3.5-layer model and (*d*) the average of two ¼° 3.5-layer model simulations. Layer two currents averaged over the same time period for (*e*) the ½° 3.5-layer model and (*f*) the average of two ¼° 3.5-layer model simulations. The reference vector above (*a*) through (*d*) is 1.0 m s^{-1} while it is 0.5 m s^{-1} for (*e*) and (*f*).

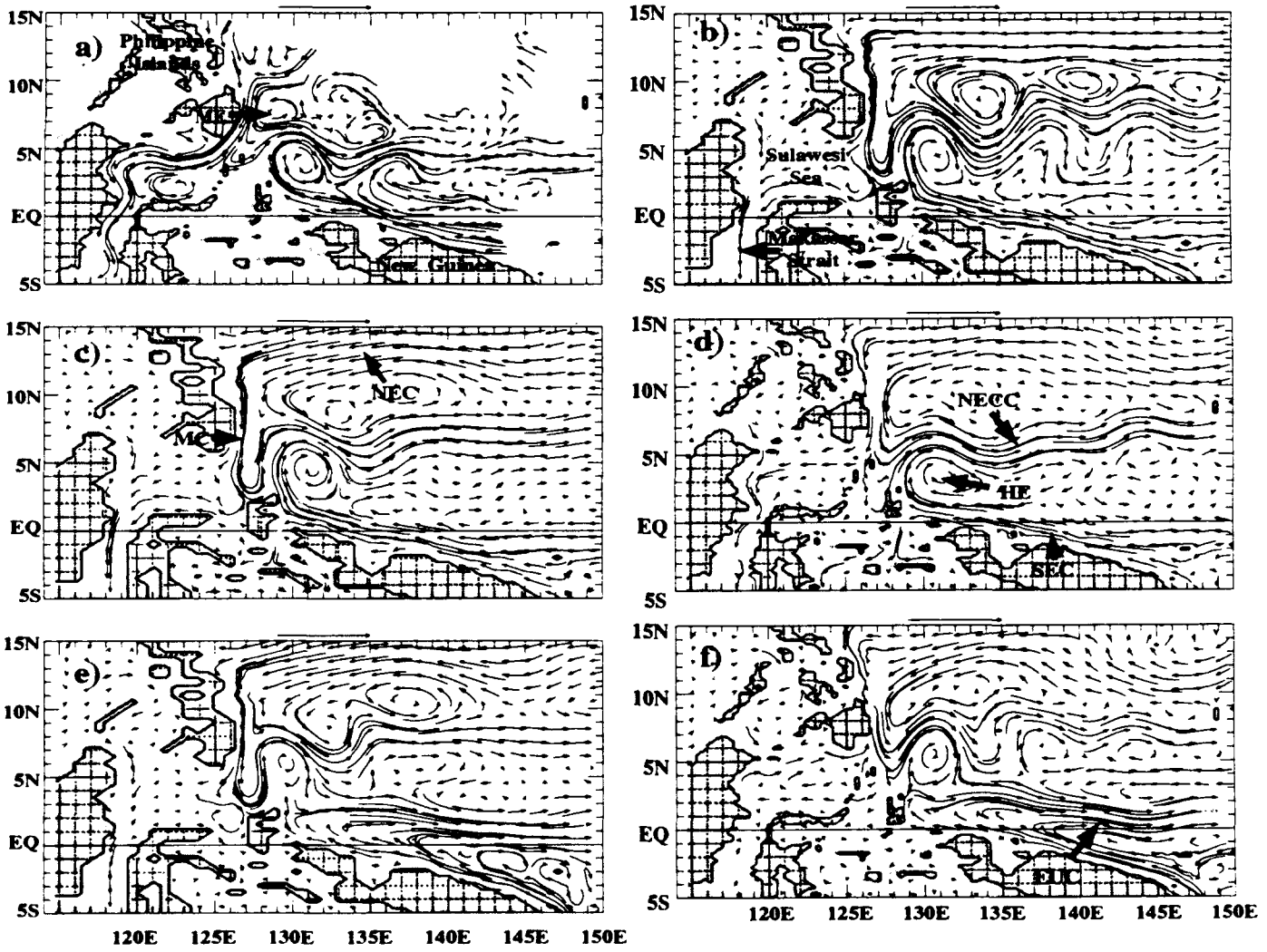

has been plotted on the model topography for ease of comparison. The upper layer currents from the models averaged over the same time period are as follows: Figure 2b, ½° 1.5-layer model; Figure 2c, ½° 3.5-layer model; and Figure 2d, ¼° 3.5-layer model.

Figures 2d and 2f are an average of two ¼° 3.5-layer model simulations. The second realization used the end point of the first as its initial state. With increased horizontal resolution and a much lower eddy viscosity (300 $m^2 s^{-1}$ versus 1,500 $m^2 s^{-1}$ for the ½° 3.5-layer model and 2,000 $m^2 s^{-1}$ for the ½° 1.5-layer model), flow instabilities are more pronounced in the ¼° model compared to the ½° models. Thus, given the same atmospheric forcing, a small perturbation in the initial state could cause the two hindcasts to differ significantly. In order to lessen these flow instability effects, an average of the two ¼° model simulations is used.

The agreement between the WEPOCS III data and the three model simulations is generally good. All show the southward flowing MC along the east coast of the Philippines and its bifurcation in the Sulawesi (formerly Celebes) Sea. The WEPOCS III data indicate the westward branch is strongest in the northern Sulawesi Sea with some recirculation in the south. The ¼° model (Figure 2d) agrees well in the region. There is some disagreement between the ½° models (Figures 2b and 2c) and the observed data concerning this westward branch. The ½° models show westward flow, which strengthens to the south, across the entire Sulawesi Sea. Despite this disagreement, all three models and the observed data indicate the MC as the primary water mass source for Pacific to Indian Ocean throughflow via the Makassar Strait. This agrees with the global simulations described in Kindle et al. (1989) as well.

The remaining branch of the MC flows southward a short distance, turns eastward around the Mindanao Eddy (ME) (8°N, 129°E in the observations and the ¼° model) and feeds the NECC. All the models depict this with some having more success than others. South of Mindanao the two ½° models (Figures 2b and 2c) have stronger southward flow than is observed and the center of the ME is too far south. The ¼° model (Figure 2d) agrees best with the WEPOCS III data south of Mindanao. This is possibly because the ¼° model is better able to resolve the complex geometry of this region. Note, both Sangihe and Talaud Islands are seen near 3°–4°N, 126°–127°E. The surface flow between these two islands is in agreement with observations reported by Wyrtki (1961).

The SEC crosses the equator along the north coast of New Guinea and is relatively strong in both the models and the observed data. Near 2°N, 134.5°E, the WEPOCS III data indicate a small northward branch emanating from the SEC that feeds the NECC. Both ½° models bifurcate at this longitude while the ¼° model does not. The main branch of the SEC joins the MC near 3°N, 128°E to help feed the NECC. North of the SEC two anticyclonic eddies appear in the observed data. The one centered near 4°N, 131°E is the Halmahera Eddy (HE). The location and shape of the HE is better represented in the two ½° model simulations. The ¼° model places the eddy slightly too far south and its shape is somewhat elongated. The anticyclonic eddy to the east of the HE is seen in all model simulations, but the position and shape varies from the observations.

The observed data show the NECC centered along 5°N. At 133°E a large meander exists with a smaller, less distinct meander at 139°E. All three models agree well with the longitudinal location of the first meander, although the amplitude varies among them. The amplitude of this meander is quite large in the ½° 1.5-layer model. With only one active layer, all the wind-driven energy is trapped in one layer and stronger currents exist. In contrast, the ½° 3.5-layer model has a smaller meander. With an increase in the number of layers, barotropic instability is decreased in this region and the energy is spread out more among the layers; weaker upper layer currents exist.

Figures 2e and 2f show the second layer currents for the ½° 3.5-layer and ¼° 3.5-layer models, respectively. These are included to show the dramatic change in the current structure between the upper two layers. In the second layer the eastward branch of the MC flows around the HE and feeds a weaker NECC. It also joins with the SEC along the north coast of New Guinea and feeds the eastward Equatorial Undercurrent (EUC). Finally, the ¼° 3.5-layer model shows a westward current near 3°–5°N, 138°–150°E, which is not present in the upper layer. It branches to feed both the NECC and the EUC.

In an effort to quantify this analysis, vector correlations were computed between the WEPOCS III data and the model results after the model data were linearly interpolated to the 1° observational grid. On the order of 250 points were used to compute the correlations. In the observations, the NECC is the dominant, strongly time-varying feature. Thus, the correlations are strongly affected by the model's positioning of this current. Those simulations that do well in positioning the NECC and the HE have higher correlations.

Table 1 shows the vector correlations between the July-August-September (JAS) 1988 drifting buoy/ADCP data and the various model JAS means for all the years of the simulations (columns 2 to 4). Here again the ¼° 3.5-layer

TABLE 1. Vector correlations between July-August-September (JAS) 1988 drifting buoy/ADCP data from Lukas et al. (1991) and the various model JAS means (columns 2–4). Vector correlations between the JAS 1988 model mean from one ¼° realization versus the various JAS model means from the second ¼° realization (column 5). Model-model correlations were limited to those points where observational data existed.

	Observations vs Model			Model vs Model
YEAR	½° 1.5 layer	½° 3.5 layer	¼° 3.5 layer	¼° 3.5 layer
1990	—	—	0.39	0.54
1989	0.48	0.57	0.53	0.60
1988	0.54	0.54	0.62	0.82
1987	0.47	0.48	0.45	0.45
1986	0.44	0.44	0.47	0.43
1985	0.52	0.53	0.45	0.47
1984	0.20	0.17	0.15	-0.01
1983	0.17	0.16	0.05	0.08
1982	0.47	0.46	0.26	0.30

model results are for the average of two realizations. Except for one case, the JAS 1988 WEPOCS III data correlate better with the model JAS 1988 mean data than with the model JAS means for the other years. This result also applies to both individual realizations of the ¼° model (not shown). The ¼° model results for 1988 are better than either of the ½° models, and the ¼° model discriminates the agreement with 1988 from the other years better than the other models. The one exception is the ½° 3.5-layer model, which produces a slightly higher correlation for the 1989 JAS model mean than for 1988; in this model the position of the NECC in 1989 is closer to the observations than the hindcast for 1988. The large year-to-year changes in the correlation with the 1988 observations demonstrate significant interannual variability in the position and strength of the NECC and the HE. It should be noted, however, that part of the interannual variability appears to result from operational changes in the ECMWF atmospheric forcing products.

Listed in column five of Table 1 are vector correlations between the JAS 1988 model mean from one realization of the ¼° model versus the JAS model mean for the various years from the second realization. The model-to-model correlation calculations were limited to those points where observational data existed. Differences between these two ¼° simulations are attributed mainly to flow instabilities. The verification year has the highest correlation (0.82). However, the off-year correlations to 1988 are very similar to the off-year observation versus model correlations (columns 2 to 4), and they exhibit the same degree of interannual variability. The correlations are only slightly improved in the off-years when comparing the JAS mean from one realization with the JAS 1988 mean from the same realization (not shown). Although the effect is small, this suggests long-term anomalies due to flow instabilities and/or long-term memory due to differences in the initial state that might influence this region. The Pacific to Indian Ocean throughflow via Indonesia is a likely contributor to this long-term memory. Although the throughflow exhibits strong seasonal variability, the annual mean throughflow is relatively slow to equilibrate due to the global origins of this feature. Also computed but not shown were year-by-year correlations between the two ¼° realizations. The 1988 value of 0.82 shown in column 5 has the median correlation for the years 1982 through 1990, which ranged from 0.73 to 0.94.

The detailed agreement among the observations and the three models is somewhat surprising, not just because of the complexity of the region but also because all of the models show the western equatorial Pacific as a region that exhibits relatively strong flow instabilities as discussed above. These have characteristic time scales of one to four months. Therefore, three months is a short time to average them out. In addition to flow instabilities and shortcomings in the models, gross differences in sampling and errors in the atmospheric forcing are other major reasons for differences between the models and the observations.

ISLAND AND COASTAL SEA LEVEL COMPARISON

The Integrated Global Ocean Services System (IGOSS) Sea Level Program makes island and coastal data available in the form of monthly means. The time series represent deviations from the 1975 to 1986 mean sea level computed for each station; all data have been quality controlled and any large linear trends have been removed. Sea level time series from the model have been extracted at the gridpoints closest to the island or coastal station. Since the model

land/sea boundary is the 200 m isobath, the sampling points may differ by up to a few degrees—a point to consider in comparing the results. The long-term mean has also been subtracted from the model sea level time series.

Comparisons between the three global models and the observed IGOSS monthly sea level data were conducted for twenty-nine island and coastal stations in the Pacific Ocean. The majority of stations are in the tropical latitudes, but a few are located at mid-latitudes (e.g., Neah Bay, Washington and Crescent City, California). Figure 3 shows the location of the IGOSS stations plotted on the model domain. The comparison for Tumaco, Colombia, a coastal station in the eastern Pacific located near 2°N, 79°W, is shown in Figure 4. The upper panel (Figure 4a) shows the IGOSS data plotted with the ½° 1.5-layer model; the lower panel (Figure 4b) shows the IGOSS data plotted with the ½° and ¼° 3.5-layer models. In this region all three models produce similar time series. In general, the models are able to reproduce the interannual sea level variations quite well. This is especially true in the example shown; the large increase in sea level associated with the 1982–83 El Niño is clearly seen in all data sets. This provides a measure of confidence in the atmospheric forcing data and in the ability of the model to respond to the forcing on these time scales.

On seasonal and intraseasonal time scales the models have mixed success. At times they are able to reproduce both the phase and amplitude of the sea level signal, but frequently both are in error. Generally, the variability about the mean is also weaker in the models than in the IGOSS data. This is probably partly due to the use of monthly mean wind forcing. Since the Nyquist frequency is two months, perhaps the best to be expected is for the models to resolve the semi-annual time scale.

To quantify this comparison, correlation coefficients between the IGOSS and model data have been computed (Table 2); the values for the ¼° model are again averages for the two realizations. If there were two realizations from the ½° model and the results were also averaged, it is expected that the correlations would be slightly higher. However, the flow instability effects would not be nearly as pronounced as they are in the ¼° simulations. The correlations are generally good, however, there are a few cases where the model does not accurately determine the sea level (Noumea and Midway). In the eastern tropical Pacific, the ½° 1.5-layer model represents observed sea level variability with accuracy equivalent to its 3.5-layer counterparts; exceptions to this are a few stations along the coast of Mexico. But the addition of multiple layers (compare columns ½° 1.5-layer and ½° 3.5-layer) leads to an overall improvement in the statistics. Most notable are Nauru and Tarawa, which are located near the equator in the Gilbert Islands.

As shown in Figure 2, a major equatorial current system is added to the model when the vertical resolution is increased from 1.5 to 3.5 layers. In the second layer, the eastward EUC and the westward currents that parallel it to the north and south are added (Figure 2f). The 3.5-layer models also produce a more realistic SEC than the 1.5-layer model. In the former, the SEC extends a few degrees into the Northern Hemisphere while in the latter the

FIGURE 3. Locations of the Integrated Global Ocean Services System (IGOSS) Sea Level Program island and coastal stations plotted on the model domain.

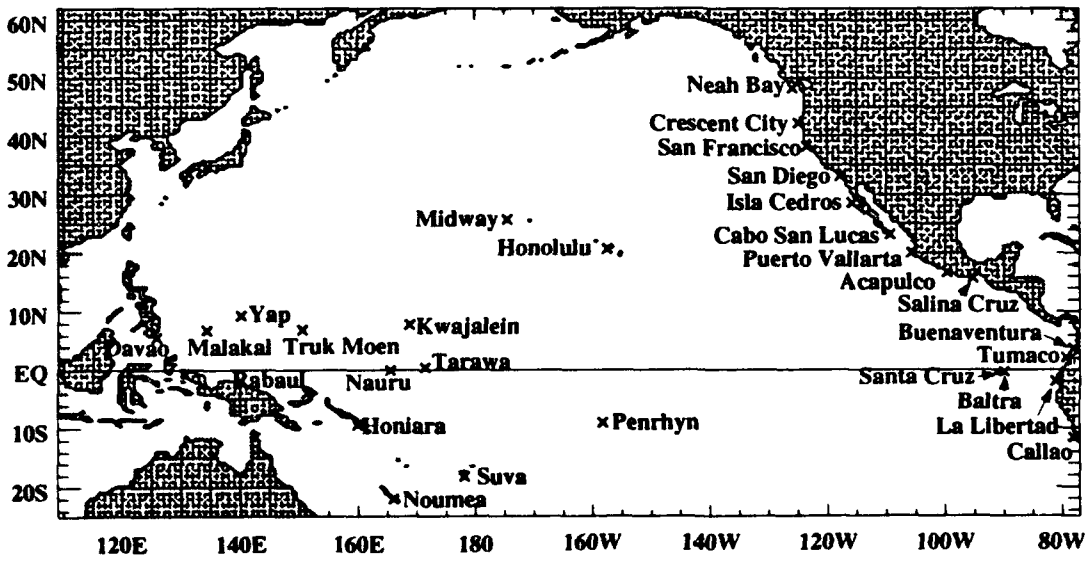

FIGURE 4. Monthly sea level data for Tumaco, Colombia (1°50'N, 78°44'W); a thirty-day running mean has been applied to the model data. (*a*) Observed Integrated Global Ocean Services System (IGOSS) data (heavy line) and the ½° 1.5-layer model (thin line). (*b*) Observed IGOSS data (heavy line), ½° 3.5-layer model (thin line) and the ¼° 3.5-layer model (dashed line).

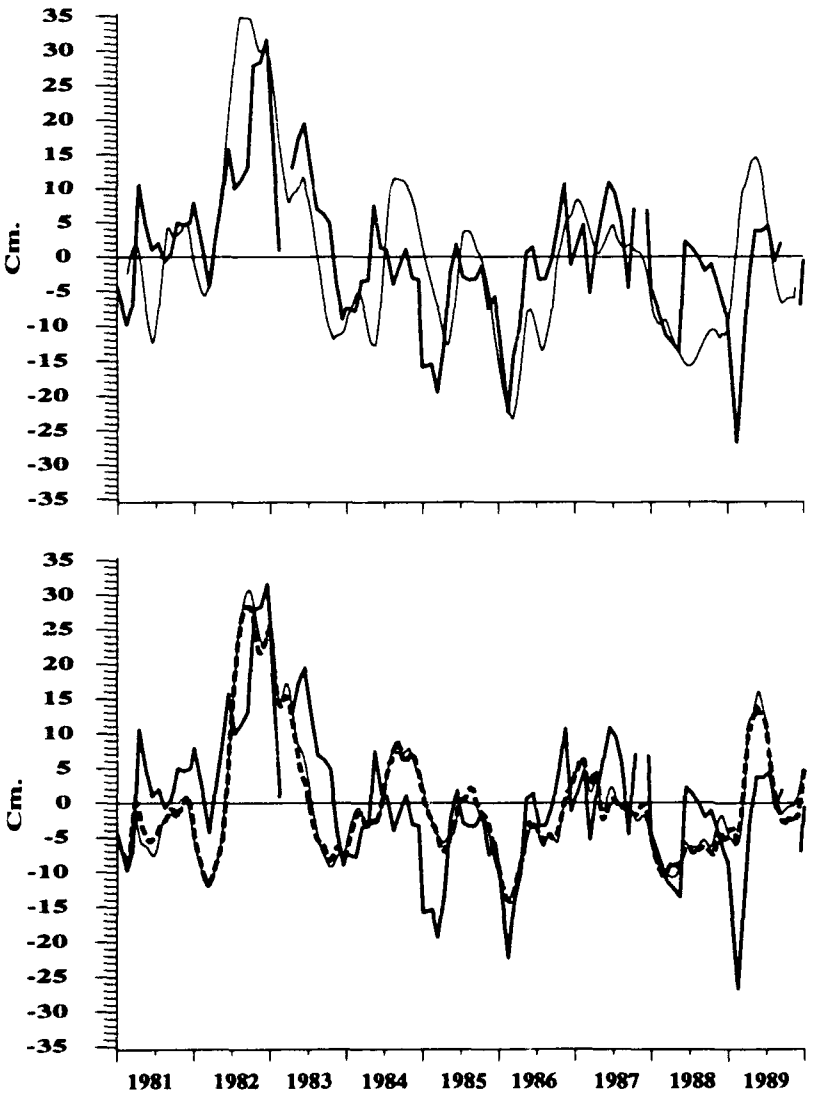

broad NECC spreads unrealistically into the Southern Hemisphere. Associated with improvements in the 3.5-layer models is an improved circulation in the Solomon Sea and a higher correlation at Rabaul.

An increase in horizontal resolution (compare columns ½° 3.5-layer and ¼° 3.5-layer) does not significantly improve the correlations. Overall, the statistics from the ¼° 3.5-layer model are equivalent to or slightly improved compared to the ½° 3.5-layer model. The higher resolution permits a greater fraction of the variability to occur in the form of flow instabilities that are not a direct response to atmospheric forcing. In some cases this leads to substantial decreases in correlation; the most serious degradation can be seen at Honolulu. This is a result of large anticyclonic eddies that propagate past Hawaii in the return flow of the subtropical gyre. These eddies have unrealistically large sea level amplitude in this model, but they are not well resolved at ½°. Nor are they found at such large amplitude in the ¼° 6-layer Pacific model with realistic bottom topography discussed by Hurlburt et al. (1992).

In order to determine the model response to interannual time scales, a twelve-month running mean was applied to the model time series and to the IGOSS stations without long data gaps, and correlation coefficients were computed (not shown). For stations in the eastern Pacific, this correlation was higher than in Table 2 at all locations. The average correlation for the monthly time series was 0.61, but the average correlation for the twelve-month running mean data was 0.82. The highest correlation, which reached 0.91, was at Crescent City, California. The stations in the western and central equatorial Pacific did not show this marked improvement in determining the interannual variability over the 1981 to 1989 time frame. The average correlations for the twelve-month running mean data were nearly identical to the average correlations for the monthly data. Analysis showed that the later years (1988 and 1989) of the time series seemed to lower the interannual correlations. When recomputed over the 1981 to 1987 time frame, the average correlations of the twelve-month running mean data for the western and central stations increased by approximately the same margin as was seen in the eastern Pacific stations.

This lowering of correlations by including time series after 1987 appears to result from an operational change to the ECMWF model-data assimilation in 1987, which increased the amplitude of the winds in the tropics. These results do not imply a decrease in the quality of the ECMWF winds due to the operational change. After an adjustment period, the observed and hindcast SSH time series appear to parallel each other at least as well as before the change. The decrease in correlation from including the period after the change results from the relative length of the time series before and after the change and the strong signal of the 1982–83 El Niño in the time series.

CONCLUSIONS

The ability of the global reduced-gravity models to hindcast wind-driven anomalies has been documented by comparing model results with various observational data sets. These include satellite altimetry, drifting buoys, and sea level data. Three models using various horizontal and vertical resolution were studied. Because these models omit the barotropic mode and are either non-eddy resolving or only

TABLE 2. Correlation coefficients between observed Integrated Global Ocean Services System (IGOSS) sea level data and the global models. The IGOSS data are monthly averages and a thirty-day running mean has been applied to the model results.

IGOSS Station	Location (Lat., Long.)	1/2° 1.5-layer	1/2° 3.5-layer	1/4° 3.5-layer
Davao, Philippines	(07°05'N, 125°38'E)	0.68	0.66	0.68
Malakal, Belau	(07°20'N, 134°28'E)	0.40	0.46	0.43
Yap, F.S.M.	(09°31'N, 138°08'E)	0.36	0.26	0.22
Truk Moen, F.S.M.	(07°27'N, 151°51'E)	0.61	0.58	0.37
Kwajalein, Marshall Is.	(08°44'N, 167°44'E)	0.54	0.54	0.33
Tarawa, Kiribati	(01°22'N, 172°56'E)	0.31	0.52	0.53
Nauru, Nauru	(00°32'S, 166°54'E)	0.24	0.47	0.46
Rabaul, P.N.G.	(04°12'S, 152°11'E)	0.75	0.83	0.83
Penrhyn, Cook Island	(09°01'S, 158°04'W)	0.71	0.76	0.77
Honiara, Solomons	(09°26'S, 159°57'E)	0.74	0.73	0.82
Suva, Fiji	(18°08'S, 178°26'E)	0.58	0.67	0.56
Noumea, New Caledonia	(22°18'S, 166°26'E)	0.25	0.29	0.21
Midway, USA Trust	(28°13'N, 177°22'W)	-0.02	0.01	0.13
Honolulu, HI	(21°18'N, 157°52'W)	0.45	0.42	0.03
Nean Bay, WA	(48°22'N, 124°37'W)	0.85	0.86	0.86
Crescent City, CA	(41°45'N, 124°12'W)	0.67	0.71	0.75
San Francisco, CA	(37°48'N, 122°28'W)	0.57	0.61	0.61
San Diego, CA	(32°42'N, 117°10'W)	0.40	0.57	0.55
Isla Cedros, Mexico	(28°11'N, 115°13'W)	0.44	0.59	0.62
Cabo San Lucas, Mexico	(22°53'N, 109°54'W)	0.38	0.56	0.56
Puerto Vallarta, Mexico	(20°37'N, 105°15'W)	0.32	0.38	0.36
Acapulco, Mexico	(16°50'N, 99°55'W)	0.54	0.52	0.54
Salina Cruz, Mexico	(16°10'N, 95°12'W)	0.36	0.44	0.44
Buenaventura, Colombia	(03°54'N, 77°06'W)	0.56	0.56	0.57
Tumaco, Columbia	(01°50'N, 78°44'W)	0.63	0.63	0.66
La Libertad, Ecuador	(02°12'S, 80°55'W)	0.64	0.62	0.66
Callao, Peru	(12°03'S, 77°09'W)	0.66	0.70	0.70
Baltra, Ecuador	(00°26'S, 90°17'W)	0.62	0.57	0.57
Santa Cruz, Ecuador	(00°45'S, 90°19'W)	0.64	0.67	0.66

marginally eddy resolving, they lack much of the mesoscale variability associated with the major western boundary currents. Due to this limitation, most comparisons were for wind-driven anomalies in the tropical latitudes.

The generally good comparison of SSH anomalies between the model and the GEOSAT-ERM indicates that the model is accurately responding to the large-scale wind driving in the tropics, a result that owes credit to the ECMWF 1000 mb winds as well. At the same time it adds credibility to the large-scale orbit error correction techniques used to process the altimetric data. On a finer scale, the models were able to represent the complex current structure of the western equatorial Pacific Ocean as indicated by comparisons with drifting buoys and ADCP data. Finally, the model's interannual variability of sea level at various tropical and mid-latitude stations compares quite well with the observed data.

The greatest improvement in the model-data comparisons came when the vertical resolution was increased from 1.5 to 3.5 layers. This allows for the formation of the EUC and a much more realistic SEC. Increasing the horizontal resolution from ½° to ¼° did not significantly improve most of the model-data comparisons presented here. The success of these comparisons depended on a relatively direct ocean model response to atmospheric forcing. Although it was shown that increasing the horizontal resolution yielded some improvements in representing currents in the western equatorial Pacific, increasing the resolution also increased the fraction of the variability due to flow instabilities, which are not a direct response to atmospheric forcing. This tends to degrade comparisons aimed at the wind-driven response. However, it is obvious that even finer resolution and the barotropic mode are needed to accurately model the mesoscale variability due to flow instabilities in the mid-latitude and subpolar regions of the world oceans. (Hurlburt et al., 1992; Hogan et al., 1992, this issue.)

ACKNOWLEDGMENTS

This work has been performed as part of the Naval Research Laboratory (NRL) 6.2/6.3 Global Ocean Prediction System projects. These are components of the Navy Ocean Modeling Program managed by Robert Peloquin under

program elements 62435N and 63207N. It is also a contribution to the NRL 6.1 Eddy-Resolving Global Ocean Model project under program element 61153N sponsored by the Office of Naval Research. Thanks are extended to Dr. Alan J. Wallcraft for his expertise in developing the global ocean model as well as Dr. Phil Richardson for providing the analysis of WEPOCS III data. Finally, we thank Ashley McManus for her work in preparing the figures. The numerical simulations were performed on the Primary Oceanographic Prediction System CRAY Y-MP 8/8128 at the Naval Oceanographic Office. This work is NRL contribution number JA 323:049:92 and has been approved for public release.

REFERENCES

Busalacchi, A.J., Takeuchi, K. and O'Brien J.J. 1983. On the interannual wind-driven response of the tropical Pacific Ocean. In: *Hydrodynamics of the Equatorial Ocean*, ed. J.C.J. Nihoul, pp. 155–195. Amsterdam:Elsevier Science Publishers.

Cane, M.A., Zebiak, S.E. and Dolan, S.C. 1986. Experimental forecasts of El Niño. *Nature*, 321:827–832.

Gordon, A.L. 1986. Interocean exchange of thermohaline water. *J. Geophys. Res.*, 91:5037–5046.

Haines, B.J., Born, G.H., Marsh, J.G. and Williamson, R.G. 1990. Precise orbit computation for the GEOSAT Exact Repeat Mission. *J. Geophys. Res.*, 95:2871–2886.

Haney, R.L. 1980. A numerical case study of the development of large-scale thermal anomalies in the central North Pacific Ocean. *J. Phys. Oceanogr.*, 10:541–556.

Hellerman, S. and Rosenstein, M. 1983. Normal monthly wind stress over the world ocean with error estimates. *J. Phys. Oceanogr.*, 13:1093–1104.

Hogan, P.J., Hurlburt, H.E., Jacobs, G., Wallcraft, A.J., Teague, W.J. and Mitchell, J.L. 1992. Simulation of GEOSAT, TOPEX/Poseidon, and ERS-1 altimeter data from a ¼° Pacific Ocean model: Effects of space-time resolution on mesoscale sea surface height variability. *Mar. Technol. Soc. J.*, (this issue).

Hurlburt, H.E. 1984. The potential for ocean prediction and the role of altimeter data. *Mar. Geod.*, 8:17–66.

Hurlburt, H.E. 1987. The ocean prediction problem and its diversity: Some issues and possible solutions. In: *Ocean Prediction Workshop 1986*, eds. C.N.K. Mooers, A.R. Robinson and J.D. Thompson, pp. 192–226. Oceanographer of the Navy, Washington D.C. and Office of Naval Research, Arlington VA.

Hurlburt, H.E., Kindle, J.C., Metzger, E.J. and Wallcraft, A.J. 1989. Results from a global model in the western tropical Pacific. In: *Proceedings of the Western Pacific International Meeting and Workshop on TOGA COARE*, eds. J. Picaut, R. Lukas and T. Delcroix, pp. 343–354. Centre ORSTOM de Noumea, New Caledonia.

Hurlburt, H.E. and Thompson, J.D. 1980. A numerical study of Loop Current intrusions and eddy shedding. *J. Phys. Oceanogr.*, 10:1611–1651.

Hurlburt, H.E., Wallcraft, A.J., Sirkes, Z. and Metzger, E.J. 1992. Modeling of the Global and Pacific Oceans: On the path to eddy-resolving ocean prediction. *Oceanography*, 5:9–18.

Kindle, J.C., Hurlburt, H.E. and Metzger, E.J. 1989. On the seasonal and interannual variability of the Pacific to Indian Ocean throughflow. In: *Proceedings of the Western Pacific International Meeting and Workshop on TOGA COARE*, eds. J. Picaut, R. Lukas and T. Delcroix, pp. 355–365. Centre ORSTOM de Noumea, New Caledonia.

Koblinsky, C., Marsh, J.G., Beckley, B., Brenner, A. and Williamson, R. 1990. GEOSAT orbit replacement software for altimeter geophysical data records. GEM-T2 ephemerides for November 1986 to November 1988. (unpublished manuscript with software).

Levitus, S. 1982. Climatological atlas of the world ocean. *NOAA Professional Paper 13*, 173 pp., Geophysical Fluid Dynamics Laboratory, Princeton, N.J.

Lukas, R., Firing, E., Hacker, P., Richardson, P., Collins, C., Fine, R. and Gammon, R. 1991. Observations of the Mindanao Current during the Western Equatorial Pacific Ocean Circulation Study. *J. Geophys. Res.*, 96:7089–7104.

Pares-Sierra, A. and O'Brien, J.J. 1989. The seasonal and interannual variability of the California Current system: A numerical model. *J. Geophys. Res.*, 94:3159–3180.

Philander, S.G. 1990. El Niño, La Niña and the Southern Oscillation. *International Geophysics Series, Vol 46*, eds. R. Dmowska and J.R. Holton, New York: Academic Press, 293 pp.

Schmitz, W.J. and Richardson, P.L. 1991. On the sources of the Florida Current. *Deep-Sea Res.*, 38:S379–S409.

Sirkes, Z. and Wunsch, C. 1990. Note on apparent systematic and periodic errors in GEOSAT orbits. *Geophys. Res. Let.*, 17:1307–1310.

Teague, W.J. and Hogan, P.J. 1989. Regional plots from the GDEM and Levitus climatologies. *NORDA Technical Note 361*, 492 pp.

Wallcraft, A.J. 1991. The Navy Layered Ocean Model users guide. *NOARL Report 35.*, 21 pp.

Wyrtki, K. 1961. Physical oceanography of the southeast Asian waters. *NAGA Report 2*, Scripps Inst. Oceanogr., 195 pp.